JACS
JOURNAL OF THE AMERICAN CHEMICAL SOCIETY

Article

pubs.acs.org/JACS

Length-Dependent Nanotransport and Charge Hopping Bottlenecks in Long Thiophene-Containing π-Conjugated Molecular Wires

Christopher E. Smith,[†,‡] Samuel O. Odoh,[†,§] Soumen Ghosh,[†,§] Laura Gagliardi,[*,†,§] Christopher J. Cramer,[*,†,§] and C. Daniel Frisbie[*,‡]

[†]Department of Chemistry and [‡]Department of Chemical Engineering and Materials Science, [§]Chemical Theory Center, and Supercomputing Institute, University of Minnesota, Minneapolis, Minnesota 55455, United States

Supporting Information

ABSTRACT: Self-assembled conjugated molecular wires containing thiophene up to 6 nm in length were grown layer-by-layer using click chemistry. Reflection−absorption infrared spectroscopy, ellipsometry and X-ray photoelectron spectroscopy were used to follow the stepwise growth. The electronic structure of the conjugated wires was studied with cyclic voltammetry and UV−vis spectroscopy as well as computationally with density functional theory (DFT). The current−voltage curves (±1 V) of the conjugated molecular wires were measured with conducting probe atomic force microscopy (CP-AFM) in which the molecular wire film bound to a gold substrate was contacted with a conductive AFM probe. By systematically measuring the low bias junction resistance as a function of length for molecules 1−4 nm long, we extracted the structure dependent tunneling attenuation factor (β) of 3.4 nm^{-1} and a contact resistance of 220 kΩ. The crossover from tunneling to hopping transport was observed at a molecular length of 4−5 nm with an activation energy of 0.35 eV extracted from Arrhenius plots of resistance versus temperature. DFT calculations revealed localizations of spin densities (polarons) on molecular wire radical cations. The calculations were employed to gauge transition state energies for hopping of polarons along wire segments. Individual estimated transition state energies were 0.2−0.4 eV, in good agreement with the experimental activation energy. The transition states correspond to flattening of dihedral angles about specific imine bonds. These results open up possibilities to further explore the influence of molecular architecture on hopping transport in molecular junctions, and highlight the utility of DFT to understand charge localization and associated hopping-based transport.

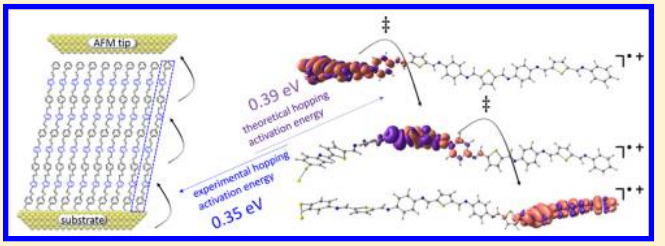

INTRODUCTION

Understanding the influence of molecular structure on charge transport over nanometer length scales is an important step toward developing devices for molecular electronics. Most of the work on molecular junctions has focused on molecules with lengths <4 nm. In this case, off-resonant tunneling is the usual charge transport mechanism, with tunneling resistances dependent on the length of the molecule in the junction (or the junction thickness), the energy offset between the Fermi energy (E_F) of the contacts and either the highest occupied molecular orbital (HOMO) or lowest unoccupied molecular orbital (LUMO) of the molecule, and the electronic overlap between adjacent units in the junction.[1−7] Charge hopping transport, however, has been much less studied in single molecules.[8−27] Previous electron transfer experiments and theoretical predictions have shown that molecular length is among the many factors affecting the charge transport mechanism in a molecular junction. When the molecule is long enough so that direct electrode-to-electrode tunneling is suppressed, and when the energies of the molecular states are close enough to the E_F of the contacts such that charge can be injected into the molecular backbone at reasonable voltages (before breakdown), charge hopping can prevail.[28−37]

In one limit, charge hopping can be viewed as adiabatic electron transfer occurring spontaneously at the intersection point of the diabatic potential energy surfaces of initial and final charge-localized (polaron) states. This intersection point is an isoenergetic point associated with a particular nuclear configuration of the overall system (the transition state) accessed through vibrational motion. In such a case, polaron transfer is an activated process where the formal activation energy is the difference between the energy of the equilibrium structure for the reference diabatic state and the energy of the system at the transition state.

Alternatively, charge hopping can also occur by thermally activated sequential tunneling of polarons within individual molecules. In this case, rather than reaching the transition state, polarons tunnel through the diabatic potential energy barriers. The process is thermally activated (e.g., because the barrier is too wide near the vibrational ground state), but the effective activation energy will be less than that predicted for semiclassical adiabatic electron transfer.[38] One of the goals of our combined experimental and computational efforts is to

Received: July 15, 2015

DOI: 10.1021/jacs.5b07400
J. Am. Chem. Soc. XXXX, XXX, XXX−XXX

understand the spectrum of factors governing these two different polaron transport regimes.

In previous work, we have shown that conducting probe atomic force microscopy (CP-AFM) can measure electrical resistance of a variety of conjugated molecular wire structures with tunable properties (length, resistance, band gap, redox potentials etc.)[39−41] and also that hopping transport occurs when molecules in the junction are longer than ∼4 nm. Since charge is injected from one contact into the molecular wire in the hopping regime and is driven through the wire's conjugated architecture by the applied electric field, it is expected that the molecular structure and HOMO/LUMO energy levels will play a key role in the transport. Because of their low ionization potentials, electron donor moieties, such as thiophene, are interesting building blocks for molecular wires.[1,42−45] In the present work, donor-containing molecular wire thin films were grown through a stepwise, self-assembled multilayer synthesis method on gold surfaces, which provides subnanometer control over the molecular length. An amine functionalized monolayer was anchored to a gold substrate with a thiol linker and π-conjugated oligophenylenethiopheneimine (OPTI) wires were grown stepwise with alternating additions of thiophene-2,5-dicarboxaldehyde and 1,4-diaminobenzene via imine-condensation click-chemistry that has been described previously.[46] Length and temperature dependent electronic characterization was performed with CP-AFM to examine the tunneling to hopping transition, Figure 1.

We found that for OPTI wires ≥4 nm in length the transport was activated, consistent with charge hopping. The activation energy was 0.38 and 0.35 eV for 4 and 5 nm wires, respectively. Notably, we performed density functional theory (DFT) calculations that support the view that charge is localized, i.e., polarons are formed. Further, the calculations uncover transition states that have energies 0.2−0.4 eV higher than the polaronic minima, in good agreement with the measured activation energies. The agreement between the measurements and DFT calculations suggests that librational motions of the wires (reciprocating torsional motion) may be important for hopping transport in the OPTI system. Further, the agreement also supports the view that for these systems the polaron transport mechanism follows the semiclassical adiabatic electron transfer picture described above.

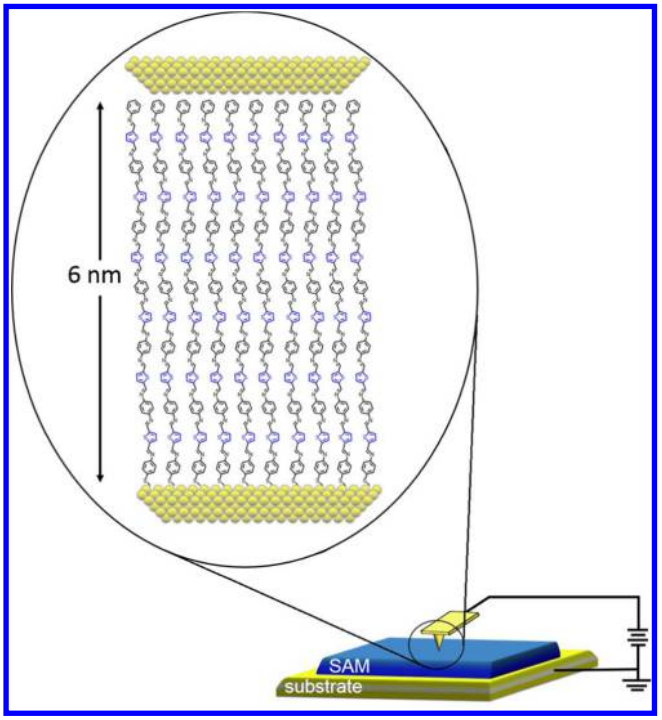

Figure 1. A schematic of an OPTI molecular junction made using CP-AFM. The thiophene donor unit is in blue. The thicknesses of the Au films on the tip and substrate are 50 nm while the SAM thickness is up to 6 nm. Given the ∼15 nm^2 contact area and measured surface coverage, it is estimated the junction consists of ∼100 molecules (see ref 47 for contact area calculations).

EXPERIMENTAL SECTION

Materials. Au nuggets (99.999% pure) were purchased from Mowrey, Inc. (St. Paul, MN). Evaporation boats and Cr evaporation rods were obtained from R. D. Matthis (Long Beach, CA). Silicon (100) wafers were purchased from WaferNet (San Jose, CA). Contact mode AFM tips (DNP or NP silicon nitride probes) were purchased from Bruker Instruments (Camarillo, CA). Absolute ethanol was obtained from Fisher Scientific and used as received. The chemicals 4-aminobenzenethiol, 1,4-diaminobenzene and thiophene-2,5-dicarboxaldehyde were ordered from Sigma-Aldrich and used as received.

Stepwise Growth and Characterization of Molecular Wires. Self-assembled molecular wires for reflection−absorption infrared spectroscopy (RAIRS), variable angle spectroscopic ellipsometry (VASE) and cyclic voltammetry (CV) were grown on thin films of 500 Å Au with a 50 Å Cr adhesion layer on a silicon (100) wafer. These metal surfaces were prepared with a home-built thermal evaporator at a rate of 1 Å/s and a base pressure of 5×10^{-7} Torr and immediately immersed in 30 mL of 1 mM 4-aminobenzenethiol (ABT) solution in argon-purged absolute ethanol. A self-assembled monolayer (SAM) of ABT was allowed to form for 18−20 h. Each sample was rinsed with 50 mL of absolute ethanol and soaked for 30 min to remove any physisorbed molecules, then dried under a stream of N_2. The growth via imine-condensation "click" chemistry was continued by alternate immersion in argon-purged ethanol solutions (30 mL, 10 mM) of thiophene-2,5-dicarboxaldehyde and 1,4-diaminobenzene for 20−24 h at room temperature with rinsing and soaking in absolute ethanol after each step. Separate samples were synthesized by alternating the addition of dicarboxaldehyde and diamine monomer molecules to lengths ranging from 1 to 12 monomers long with single monomer increments. When the desired length was reached the wires were protected from further reactions by capping the even number wires (carboxaldehyde terminated) with phenylamine and the odd number wires (amine terminated) with benzaldehyde. Capping also provides a consistent contact group for the AFM tip.

Thickness measurements of the OPTI wires were carried out by variable angle spectroscopic ellipsometry (J. A. Woollam Co., Inc.). To do this, measurements of the polarization angles (Ψ and Δ) were recorded as a function of wavelength (λ) from 800 to 1100 nm with 15 nm steps and an incident angle of 65° from surface normal. Prior to SAM formation, the indices of refraction ($n(\lambda)$) and extinction coefficients ($k(\lambda)$) of the bare Au-coated substrates were found by measuring the polarization angles at three separate locations on each substrate. After the wires were grown, the polarization angles were measured again at the same three locations. Thicknesses were fit through regression analysis to a three-layer model comprised of the silicon substrate, Au film and a Cauchy layer as the organic SAM with the VASE software. The refractive index of the SAM was fixed to 1.45 according to usual values for organic monolayers[48,49] and k to 0 because there was no absorption of the OPTI SAMs in the 800−1100 nm range. The software used the new Ψ and Δ values to calculate the molecular film thickness.

XPS spectra were taken on a SSX-100 XPS (Surface Science) (<10^{-9} Torr) with a Al Kα X-ray monochromatic source (1486.3 eV) and a hemispherical analyzer. The X-ray anode was operated at 200 W, and the analyzer was set to a pass energy of 150 eV for survey scans

DOI: 10.1021/jacs.5b07400
J. Am. Chem. Soc. XXXX, XXX, XXX−XXX

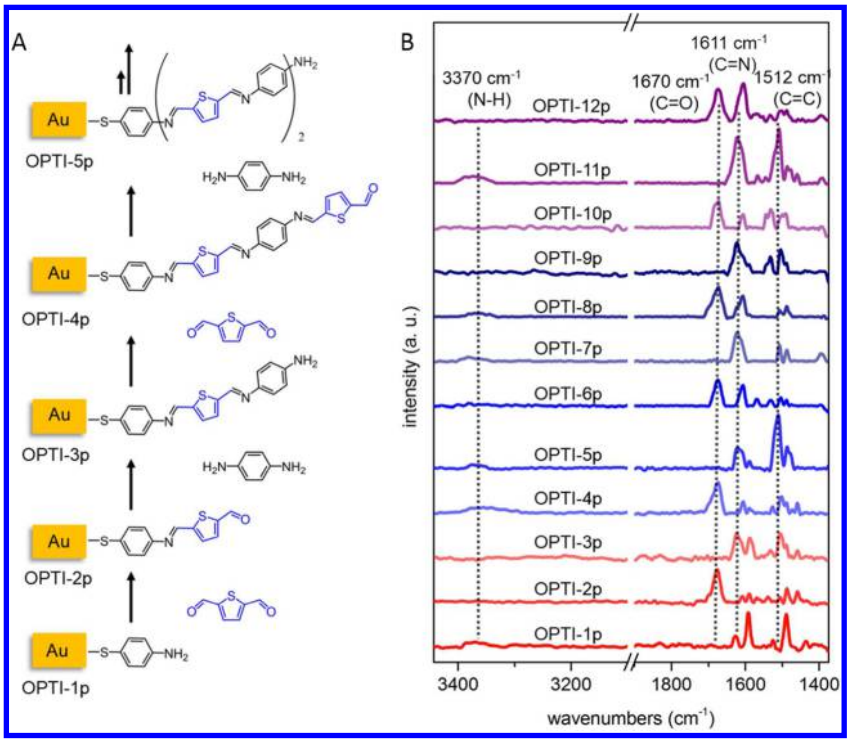

Figure 2. (A) Reaction schematic for the first five precursor (uncapped) molecular wires (OPTI-p) self-assembled onto Au surfaces. (B) RAIRS spectra for all precursor molecular wires.

and 50 eV for high-resolution scans. The binding energy scales were referenced to the Au $4f_{7/2}$ peak (84.0 eV).

Step wise progress of the OPTI wire growth was monitored with RAIRS (Nicolet Series II Magna-750 FTIR equipped with a Harrick Seagull accessory) with an incident angle of 84° from the surface normal. After each reaction, the SAM was rinsed, soaked for at least 30 min, dried under nitrogen flow, then immediately placed into the FTIR compartment and purged with N_2 for 15 min before acquiring spectra. Each sample was scanned 500 times at 2.0 cm^{-1} resolution.

The redox states and surface coverages were determined from cyclic voltammetry measurements of the OPTI wires and ferrocene-capped versions of the even OPTI wires (OPTI-Fc). The even length wires were capped with 2 mM aminoferrocene in ethanol in an inert environment for 24 h. A three-neck electrochemical cell, with a 0.9 cm diameter opening at the bottom, was placed on the sample and sealed with an O-ring. The electrolyte solution was 0.1 M $[Bu_4N^+][PF_6^-]$ (tetrabutylammonium hexafluorophosphate) in either dimethyl sulfoxide (DMSO) or acetonitrile, deoxygenated by three freeze–pump–thaw cycles. Cyclic voltammetry of the bare OPTI wires was performed in DMSO as this was found to give more pronounced oxidation peaks. The working electrode was the sample, and the counter and reference electrodes were Pt wire and Ag wire, respectively. Each sample was cycled at sweep rates between 25 and 400 mV/s through a potential window of +1 V to −2.5 V relative to the Ag wire, and the resulting voltammograms were referenced to the ferrocene/ferrocenium (Fc/Fc^+) redox couple on a separate polished Au disc electrode.

Optical absorption spectra of the wires were measured on a Spectronic GENESYS-5 UV–visible spectrophotometer from 250 to 1000 at 1.0 nm resolution. Semitransparent samples were prepared according to our previously reported method.[40]

Electrical Characterization of Molecular Junctions by CP-AFM. Metal-molecule-metal junctions were formed by touching a Au-coated AFM tip onto the capped molecular wire arrays in contact mode. The junctions were formed and high bias curves for OPTI-2 through 5 were collected on a Multimode AFM (Veeco Instruments) in a glovebox (<1.5 ppm of O_2) using a Keithley 6517A electrometer and 236 source meter controlled by LabView code. High bias $I-V$ curves were collected for OPTI-6 through 12 using an environmentally controlled Agilent Molecular Imaging PicoScan/PicoSPM equipped with a current sensing scanner and temperature control from 250 to 338 K. The Picoview software was used to simultaneously operate the AFM and perform $I-V$ measurements. Low bias curves for resistance calculations were collected on the PicoSPM except for OPTI-2, in which the current was above the 10 nA limitation even at very low bias. The Au-coated tips were prepared by the same thermal evaporation method as described above for the preparation of the SAM substrates. The substrates for AFM measurements were prepared with a template-stripping method (Au^{TS}).[17,18] All electrical measurements were performed with a 2 nN load on the AFM tip to ensure a consistent top contact. Current–voltage curves were obtained by biasing the tip relative to the substrate, where positive bias at the tip is designated forward bias. The high bias voltage range used was ±0.5 V for OPTI-2 and 3, ± 1 V for OPTI-4 to 12. For each wire length, $I-V$ curves were sampled from 4 to 6 different locations, with 25–50 sequential curves taken at each location. Reported $I-V$ curves are an average of all traces with no data selection. The low bias resistance was calculated from the linear portion of the curves within ±0.2 V. Resistance histograms are shown in the Supporting Information. A total of six AFM tips were used in the room temperature measurements of all the wire lengths, and each gave a tunneling resistance on the order to 10^8 Ω through a nonanethiol SAM standard on Au^{TS}. Variable temperature $I-V$ measurements were made on the environmentally controlled PicoSPM at <1% relative humidity. An additional three AFM tips were used to acquire all temperature dependent curves, with each length measured with a separate, freshly prepared tip. The high bias curves for OPTI-4, 6, and 8 were collected starting from 250 K up to 338 K in ~10 K increments. Each reported curve is an average of 200–300 traces sampled over 4–6 locations to ensure a statistically relevant picture of the temperature dependent $I-V$ characteristics.

Computational Methods. The geometries of the OPTI wires (n = 1–8) including one gold atom as the contact at the thiolate terminus were optimized at the density functional level of theory with the M06-HF[50,51] functional. We considered both the neutral nanowires as well as their radical cations while using basis sets of double-ζ quality including polarization functions (DZP) for all C, H, S, O and N atoms.

DOI: 10.1021/jacs.5b07400
J. Am. Chem. Soc. XXXX, XXX, XXX–XXX

The gold contact atom was described using all-electron triple-ζ polarized (TZP) basis sets. As a result of the presence of the gold atom, scalar relativistic effects were included with the Zeroth Order Regular Approximation.[52,53] The ADF package was used for all the calculations.[54] Vibrational frequency analyses were performed on all optimized geometries to confirm their nature as local minima or transition-state structures.

For the longer OPTI wires, we anticipated that many structures would be close in energy to the global minimum. Thus, we generated several starting structures for each OPTI nanowire by carrying out up to 5 ps *ab initio* molecular dynamics (AIMD) simulations and selecting snapshots therefrom (additional details are given in the Supporting Information). The dispersion-corrected PBE-D3[55−57] model was used for these simulations and the gold atom was replaced with a proton for simplicity. From each OPTI wire trajectory, 10 random snapshots were selected and these geometries were optimized at the M06-HF level after reintroduction of the gold contact atoms (placed an appropriate distance along the antecedent S−H vector).

Vertical electronic excitation energies of the neutral wires were computed using time-dependent density functional theory (TDDFT)[58] for the 10 optimized geometries of each OPTI system; for these calculations the M06 functional was used with triple-ζ basis sets with two polarization functions (TZ2P) for all atoms.[59] Singlet−singlet transitions to the first seven excited states were considered in the TDDFT calculations. This excitation window is sufficient to encompass the optical gap.[58]

To characterize the radical cationic states of each OPTI nanowire, the spin densities were computed at the M06-HF/TZP level of theory. With 100% exact exchange, the M06-HF functional is expected to minimize spurious delocalization of spin densities resulting from DFT self-interaction error. The geometries of the same 10 trajectory snapshots employed for the neutral wires were optimized at the M06-HF/TZP level for the radical cations. In addition, during the geometry optimizations, we enforced localization of the unpaired electron in different parts of each wire by specifying occupation numbers for component fragments of wires, prior to allowing the electronic structure to relax fully. For longer wires, this procedure led to additional structures beyond the initial 10 snapshots obtained from the AIMD simulations (up to 30 in the case of OPTI-8).

RESULTS AND DISCUSSION

Growth and Characterization of Molecular Wires. The OPTI molecular wire SAMs were grown in a stepwise manner using imine condensation reactions which preserve and extend the conjugation of the wire via monomer addition. The reaction schematic in Figure 2A demonstrates the alternating addition of the thiophene-2,5-dicarboxaldehyde (the donor) and 1,4-diaminobenzene monomers. Figure 2B displays the RAIRS spectra of the uncapped (OPTI-p = precursor) wires. The alternating appearance and disappearance of the carbonyl stretches (1670 cm^{-1}) and the increasing relative intensity of the imine stretching (1611 cm^{-1}) indicate a high-yield surface reaction and are consistent with the expected growth chemistry. The symmetric amine stretching (3370 cm^{-1}) and a benzene ring vibration mode (1512 cm^{-1}) are also visible in the spectra. The SAM thicknesses measured by VASE are shown in Figure 3 along with the theoretical molecular lengths. The theoretical length was estimated by addition of individual lengths for monomer units derived with ChemBio3D software and assembled into fully extended structures with all-cis configurations for the thiophene-2,5-dicarboxaldehyde. An Au−S bond length of 2.36 Å was assumed.[60] The ellipsometry data suggest a negligible SAM tilt angle except for the longest wires.

XPS was also employed to analyze sulfur content in the SAMs. Each high-resolution spectrum was background-corrected using the Shirley method[61] and the peaks were fit with 80% Gaussian-20% Lorentzian line shapes. High-resolution XPS scans were taken in the S_{2p} region to monitor the photoelectron emission signals from the thiol anchoring group and the thiophene unit (Figure 3). The S_{2p} spectra of the shorter wires show photoelectron peaks for the sulfur in the thiophene and the surface-linker at 164 and 162 eV, respectively. The intensity of the sulfur-linker peak at ∼162 eV becomes less apparent in the spectra of the longer wires due to attenuation of the photoemitted electrons as SAM thicknesses increased. See Figure S1 for XPS spectra of all even wire lengths.

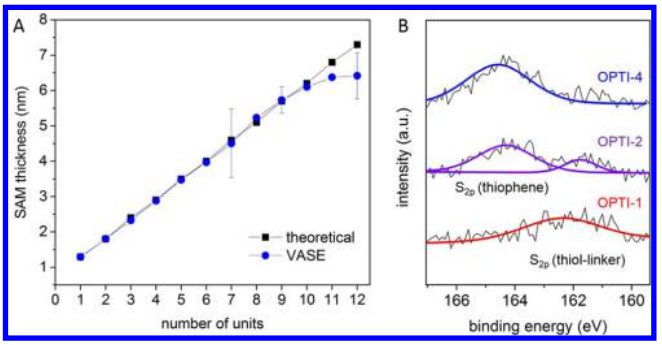

Figure 3. (A) The measured thicknesses at each step of the OPTI wire growth. The black squares are the estimated thickness assuming molecule orientation normal to the surface. Blue circles represent an average thickness of three locations on each sample. The error bars are one standard deviation and are small in most cases. (B) High-resolution XPS spectra in the S_{2p} region for OPTI-1,2 and 4 wires. The black lines are the experimental data and the colored lines are the fits.

The surface coverage of the OPTI wires was estimated by cyclic voltammetry. The even length wires were capped with aminoferrocene instead of phenylamine. This step provided a reliable one-electron redox tag for capped wires with a redox potential that was independent of wire length.[62] The oxidation peaks in the OPTI-Fc voltammograms were used to calculate the capped wire surface coverage in molecules/nm^2 (Table 1) using eq 1,

$$\Gamma = \frac{Q}{nFA} \quad (1)$$

where Q is the charge injected into the molecular wires, n is the number of electrons involved in the electron-transfer process, F is the Faraday constant, and A is the surface area of the sample exposed to the electrolyte (in this case ∼0.78 cm^2). The charge injected was determined by integrating the first oxidation peak in the cyclic voltammogram for each sweep rate. The average coverage of the OPTI-Fc was 1.3 ± 0.3 molecules/nm^2 calculated from the 100 mV/s scan rates. The extent of reaction for the ferrocene capping step has been extensively studied by Demissie et al. using XPS and Rutherford backscattering spectrometry (RBS).[63] It was found that on average only 50% of aldehyde-terminated molecular wires were capped with the aminoferrocene. In this case, if the ferrocene-capped surface coverage in Table 1 only represents half of the actual surface coverage, then the OPTI-Fc values become much closer to the coverages found from the uncapped wire oxidation peaks (Figure S2).

The cyclic voltammograms of OPTI-Fc wires capped with aminoferrocene are shown in Figure 4 and Figure S4 in Supporting Information. Voltammograms of bare OPTI wires are shown in Figure S2, and the onset potentials of the first oxidation for each OPTI length are listed in Table 1. The first

DOI: 10.1021/jacs.5b07400
J. Am. Chem. Soc. XXXX, XXX, XXX−XXX

Table 1. Properties of OPTI Wires Obtained from Surface Characterization[a]

monolayer	molecular length (nm)	film thickness (nm)	first oxidation onset potential (vs Fc/Fc^+)	surface coverage via wire ox Γ_{OPTI} (molecule/nm^2)	surface coverage via Fc capping $\Gamma_{OPTI\text{-}Fc}$ (molecule/nm^2)
OPTI-2	1.8	1.8	0.00	1.7	1.4
OPTI-4	2.9	2.9	−0.01	2.1	0.8
OPTI-6	4.0	3.9	−0.05	2.0	1.6
OPTI-8	5.1	5.2	−0.08	3.3	1.3
OPTI-10	6.2	6.1	−0.02	3.2	1.1
OPTI-12	7.4	6.4	−0.10	3.0	0.9

[a]The oxidation potentials were determined from the onset potential of the first oxidation peak.

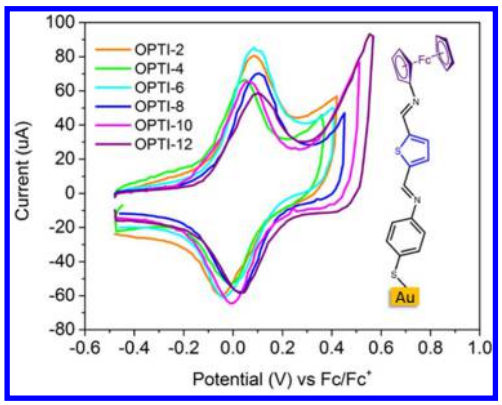

Figure 4. Cyclic voltammograms of even OPTI-Fc wires capped with aminoferrocene on Au. The electrolyte was $[Bu_4N^+][PF_6^-]$ (tetrabutylammonium hexafluorophosphate) in acetonitrile with a Ag wire and Pt wire as the reference and counter electrodes, respectively. All the scan rates were 300 mV/s. The inset shows the structure of OPTI-2p capped with aminoferrocene.

length incorporating the thiophene unit (OPTI-2) has a −200 mV shift relative to that of the analogous oligo-phenyleneimine wire (OPI-2) reported previously.[39] This was expected due to the OPTI donor character. However, there is only a small negative shift in the oxidation peak with increasing wire length, suggesting that charge delocalization is restricted to about 3 monomer units, rather than across the entire length of the molecule.

To rationalize this observation, we examined the HOMOs of the lowest energy geometries of the OPTI-n (n = 1−8) nanowires optimized at the M06-HF/TZP level of theory (Figure 5). The HOMO in OPTI-1 is delocalized over the entire nanowire, as is true also for OPTI-2. In OPTI-3, there is very little contribution (7.8%) to the HOMO from the benzaldimine cap, even though there is strong delocalization over the first three rings. For OPTI-4 and OPTI-5, there is also very little delocalization of the HOMO beyond the first three rings (10.3% and 6.9%, respectively). This suggests that the π character of the HOMO changes very little beyond OPTI-3; i.e., it is 87−93% localized over the first 3 rings from OPTI-3 to OPTI-8. Also shown in Figure 5, theory predicts a convergence in the eigenvalues of the frontier π and π^* orbitals in the longer OPTI-n wires (and thus the gap between these orbitals, a quantity approximately equivalent to the difference in the gas-phase ionization potentials and electron affinities of the wires). Thus, the calculated π−π^* gaps in the gas phase are 8.60 and 7.93 eV for OPTI-1 and OPTI-2, respectively, while the gaps for n = 3−8 are all within 7.47−7.62 eV. This convergent behavior is consistent with the observed convergence of the optical gaps and redox potentials after three monomer units. There are two additional points to note. First, this convergence of the calculated π−π^* gaps is also apparent at the PBE/TZP, M06-L/TZP and M06-2X/TZP levels of theory, see Table S1. Second, as shown in Table 1, the first oxidation onset potentials of the OPTI-n (n = 2, 4, 6, 8, 10 and 12) wires are about 0.10 eV away from that of the Fc/Fc^+ couple. At the M06-HF/TZP level of theory, the eigenvalues of the HOMOs of OPTI-n (n = 1, 2, 3, 4 and 5) are around −9.0 eV, in contrast to the HOMO of ferrocene found at around −5.0 eV. At the PBE/TZP and M06-L/TZP levels, there is a better match at around −5.0 to −5.7 eV for the calculated eigenvalues of the HOMOs of the OPTI wires and ferrocene. PBE and M06-L however lead to

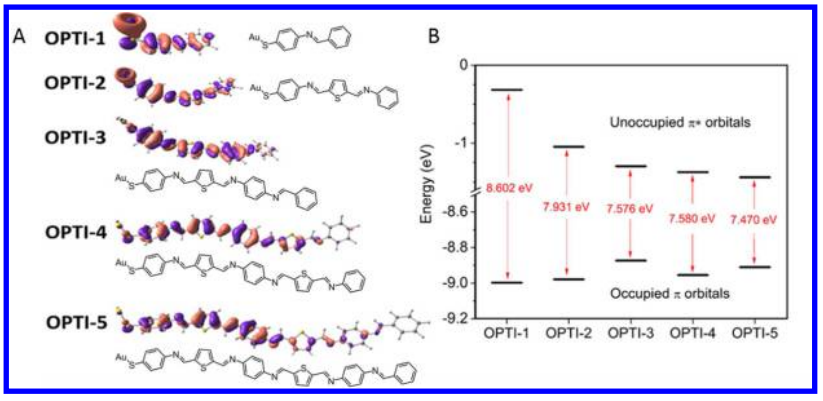

Figure 5. (A) HOMOs of OPTI-n (n = 1−5) wires for lowest energy structures obtained at the M06-HF/TZP level. (B) Corresponding calculated eigenvalues (and gaps) of the frontier π and π^* orbitals (0 eV corresponds to vacuum). The lowest π^* orbitals are of LUMO+1 character. The HOMO−LUMO separations reflect Koopmans theorem differences in ionization potentials and electronic affinities, and as such they are not directly comparable to experimental quantities measured here, but trends observed in the frontier orbital separation mimic those both measured and predicted for optical gaps, for example, and are presented here for completeness.

DOI: 10.1021/jacs.5b07400
J. Am. Chem. Soc. XXXX, XXX, XXX−XXX

delocalization of frontier orbitals across the lengths of all the OPTI wires. To remove this delocalization error, we have favored the use of the M06-HF functional in most of our computations. The UV−visible spectra of all OPTI wires are shown in Figure S6. The OPTI-1 absorption peak onset appears at ∼3.6 eV (∼340 nm), but as the OPTI wires grow longer, the $\pi-\pi^*$ transition shifts to a λ_{max} of 2.9 eV (∼430 nm). It is interesting to note that the absorption does not shift much after OPTI-3, indicating again that there is not a significant amount of delocalization beyond 3-rings. Table 2 shows that the optical band gap decreases from 2.5 to 2.3 eV, measured assuming onsets of long- wavelength absorptions corresponding to 0−0 vibrational transitions. According to the TDDFT calculations at the M06/TZ2P level, there is a low energy S1 state associated with very low oscillator strength S 3p $n-\pi^*$ transitions that is predicted at about 2.04−2.13 eV (608−582 nm), but the most intense transitions are of $\pi-\pi^*$ character and are found at 2.31−2.56 eV (537−484 nm). As we obtained several optimized structures for each OPTI wire, there is a range (usually about 0.02−0.11 eV wide) within which the most intense $\pi-\pi^*$ transitions of each nanowire are found, consistent with broadened experimental peaks associated with ensemble populations. Consistent with the voltammetry results presented in Figure S2 and Table 1, the energies for the bright S2 $\pi-\pi^*$ excitations are largely converged by OPTI-3: 2.49−2.52 eV for OPTI-1, 2.52−2.56 eV for OPTI-2, and a steady 2.31−2.45 eV for the longer wires. We note that identical trends in the calculated excitation energies of the nanowires are computed with the PBE, M06-L, and M06-HF functionals, although, as expected, the magnitudes of the excitation energies themselves are under- and overestimated, respectively, by the functionals incorporating 0% and 100% exact exchange. In addition, the calculated optical gaps obtained with TDDFT (2.35−2.52 eV at the M06/TZP level), Table 2 and Table S2, are generally lower than the calculated HOMO−LUMO gaps (3.28−4.26 eV at the M06/TZP level). This is expected as the electron and hole are bound by Coulombic interactions in the excited states described with TDDFT.[64]

Table 2. Optical Gaps (eV) Obtained from Experiment (Obtained from the Edge of UV−Visible Absorption Spectra) and Theory (The First Computed Bright Transition Involving the π Framework)

		DFT	
monolayer	expt.	lowest energy structure	range for all optimized structures
OPTI-1		2.52	2.50−2.52
OPTI-2	2.53	2.54	2.51−2.54
OPTI-3		2.46	2.39−2.47
OPTI-4	2.49	2.44	2.38−2.45
OPTI-5		2.43	2.33−2.43
OPTI-6	2.37	2.38	2.31−2.41
OPTI-7		2.42	2.34−2.45
OPTI-8	2.31	2.41	2.35−2.41

Electrical Characterization of Length Dependent Resistance. The charge transport characteristics of the OPTI wires were studied using CP-AFM. A semilog plot of low bias resistance versus length for the series of wires is shown in Figure 6. For each wire length ∼100−200 $I-V$ curves were used in the resistance calculations which were on average 92% of the collected curves (Figure S7). Because of drift in the AFM tip position and defects in the SAM, a small number of curves (∼8%) collected exhibited very high resistance and were not used in the resistance calculations (8% of the data points were omitted from the average resistance calculation, but no $I-V$ curves were omitted from the average $I-V$ curve). A transition in the transport mechanism from tunneling to hopping can be detected by a change in the length dependence of the resistance. Figure 6 shows that the resistance of OPTI-2 through OPTI-6 increases exponentially with length, whereas the length dependence of OPTI-7 through OPTI-12 is linear. As expected based on our previous results, the tunneling-to-hopping transition occurs near 4 nm.[39−41] For molecular wire lengths under 4 nm, the charge transfer can be described by the off-resonant tunneling process with eq 2,

$$R = R_0 \exp(\beta L) \tag{2}$$

where R is the junction resistance, R_0 is the effective contact resistance, L is molecular length, and β is the tunneling attenuation factor, which in molecular wires depends on the nature of bonding in the molecular backbone and is sensitive to the metal-molecule electronic coupling of the junction. The β value obtained from a linear fit of the short wire resistances is 3.4 nm^{-1}, which is in the range of values typically found in conjugated molecular wires.[65−67] For wires longer than 4 nm, the resistance increases linearly with length which is consistent with a hopping transport mechanism described by eq 3,

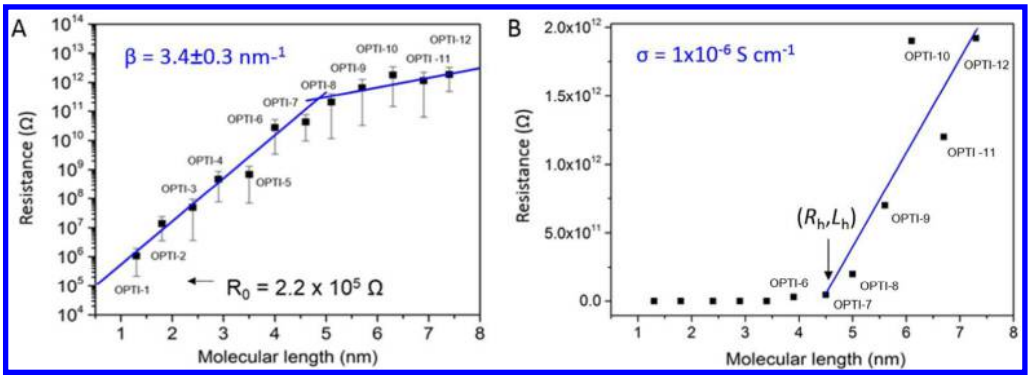

Figure 6. (A) Semilog plot of low bias resistance versus OPTI molecular wire length by CP-AFM obtained from the ±0.2 V bias range. Error bars are one standard deviation and lines are fits to the data using the least-squares method. The line fit to the wires shorter than 4 nm was used to extract β. (B) The same resistance data plotted on a linear scale. The line fit to wires longer than 4 nm was used to calculate the long wire conductivity (σ). R_h and L_h represent the resistance and molecular length at which the linear fit to hopping wires begins.

DOI: 10.1021/jacs.5b07400
J. Am. Chem. Soc. XXXX, XXX, XXX−XXX

$$R = R_h + \alpha_\infty (L - L_h) \exp\left(\frac{E_a}{k_B T}\right) \quad (3)$$

where, R_h is the resistance at which hopping begins, α_∞ is a molecule-specific parameter with units of resistance per unit length, L is the molecular length, L_h is the length at which hopping begins, E_a is the hopping activation energy, k_B is Boltzmann's constant, and T is the temperature. A linear fit to the longest six wires was used to extract the parameters in eq 3: $R_h = 4.6 \times 10^{10}$ Ω, $L_h = 4.5$ nm and the hopping attenuation factor, $\alpha_\infty = 6.4$ Ω nm^{-1}. Also the slope of the linear fit was used to obtain the long wire conductivity of 3×10^{-7} S cm^{-1} (see Supporting Information for this calculation). This is more than 10 times lower than our reported conductivity with the oligophenyleneimine (OPI) wires,[39] and is discussed below.

The high bias $I-V$ characteristics were investigated as well to see how the overall current magnitude depends on length. Figure 7 shows that the current at all biases decreases with

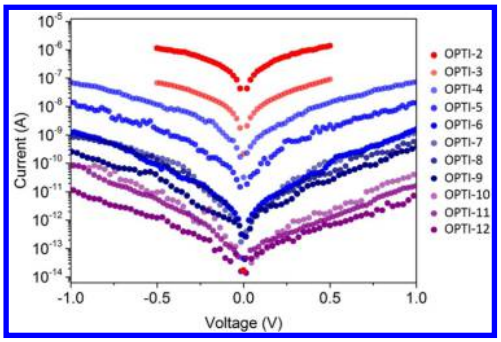

Figure 7. Semilog plot of $I-V$ curves for each molecular length. Each curve represents the average of 100 $I-V$ traces for OPTI-2 to 5 and 200−300 $I-V$ traces for OPTI-6 to 12.

increasing length, consistent with Figure 6. For wires under 4 nm, a steep decrease is visible with the trend diminishing for wires longer than OPTI-6.

Temperature-Dependent Resistances. Low-bias resistance measurements of the molecular wires over a large temperature range are useful for determining the transport mechanism. Charge tunneling typically exhibits little temperature dependence. In contrast, charge hopping requires injection of charge into the molecule from the contacts, with discrete molecular radical cation intermediates (polarons) implicated in the net charge transport. The activation energy for this process can be extracted from an Arrhenius plot of resistance versus temperature. Figure 8 displays the low-bias resistance measured at various temperatures from 250 to 338 K for selected wires. The resistances for OPTI-4 are weakly dependent on temperature, while OPTI-6 (see Figure S9) and OPTI-8 show thermally activated transport, indicating a hopping mechanism for wires over 4 nm. An Arrhenius plot showing activation energies decreasing with increasing bias is shown in Figure S10. Temperature dependent resistances for OPTI-10 and 12 were not acquired because measured currents at temperatures <300 K approach the limit of the PicoSPM current sensing capabilities.

Nature of the Charge Carriers. The switch of the hole transport mechanism from tunneling to hopping near 4 nm is interesting from a computational perspective, as the polarons of the radical cations might be localized over different subregions for different optimized geometries of each OPTI wire. Our

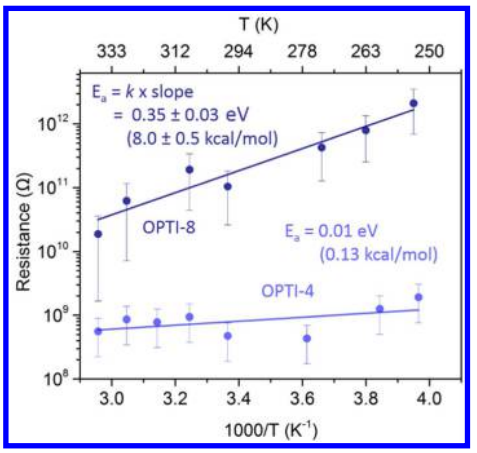

Figure 8. Arrhenius plot for OPTI 4 and 8. Each data point is the average differential resistance of a total of 200−300 curves measured at four different locations in the range of ± 0.2 V. Error bars represent one standard deviation, and activation energies are obtained from linear fits to the data.

choice of random snapshots obtained from a 5 ps AIMD simulation should, in principle, provide an opportunity to identify such different local minima. First, we examined the localization of the unpaired electron in different optimized structures of OPTI-4$^{+\bullet}$. We then compared OPTI-4$^{+\bullet}$ with OPTI-8$^{+\bullet}$, in an effort to illuminate the differences in the charge transport mechanism between the longer wire(s) and the shorter wire. Figure 9 shows the calculated spin densities

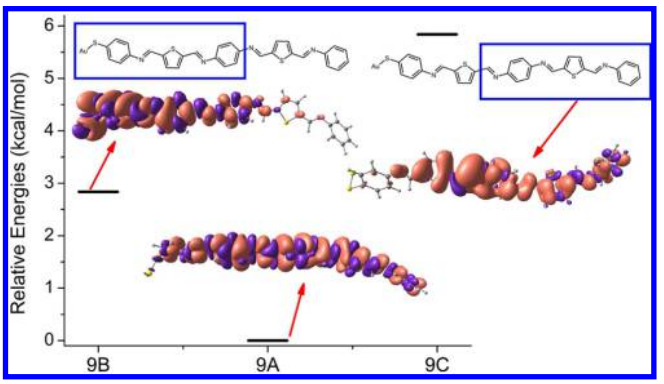

Figure 9. Spin densities of three low-energy structures of the radical cation OPTI-4$^{+\bullet}$ obtained with the M06-HF/TZP level of theory. In **9A**, the spin is delocalized over the entire wire. In **9B** and **9C**, the spin is localized over three rings. **9A** is the most stable local minimum structure obtained for the radical cation OPTI-4$^{+\bullet}$. The blue boxes highlight the region of the structure where most of the spin density is localized.

for three low energy structures of the radical cation OPTI-4$^{+\bullet}$. In the lowest energy structure (labeled as **9A**), the spin density is delocalized across the entire wire. At 300 K, **9A** is the global minimum in enthalpy; 16 other structures were found with relative enthalpies ranging from 2.04 to 11.60 kcal/mol (0.09−0.5 eV). Two additional structures were generated by enforcing localization of the spin density on either the first three rings (**9B**) or the last three rings (**9C**) while reoptimizing the geometry of **9A**. At 300 K, **9A** is calculated to be about 3.76 kcal/mol (0.16 eV) more stable than **9B** and 5.84 kcal/mol (0.25 eV) more stable than **9C**. These results suggest a strong preference for a delocalized state in OPTI-4$^{+\bullet}$. While this is

DOI: 10.1021/jacs.5b07400
J. Am. Chem. Soc. XXXX, XXX, XXX−XXX

consistent with a single step tunneling mechanism, it is generally agreed that the charge does not spend time on the short wires.

Figure 10, in contrast, shows calculated spin densities for various structures obtained for the radical cation OPTI-8$^{+\bullet}$. The lowest energy structure, **10A**, has spin density localized across its first three rings. In other local minima, the spin density is also localized over discrete subregions of the nanowire, i.e., no structure was obtained in which the spin density is predicted to be delocalized over the entire wire. This was found to be true even for structures with all heavy atoms forced to be coplanar to optimize conjugated overlap. Such geometries were predicted to be transition-state structures on the potential energy surface, but nevertheless showed spin localization. For hole transport to occur in OPTI-8$^{+\bullet}$, the polaron localized on the first three rings in **10A** must migrate the length of the nanowire. We found several low-energy structures in which the spin density is localized on either the second or third set of three rings, with the most stable (**10B** and **10C**) shown in Figure 10. Higher energy structures were also found, including some with localizations on other possible 3-ring subregions.

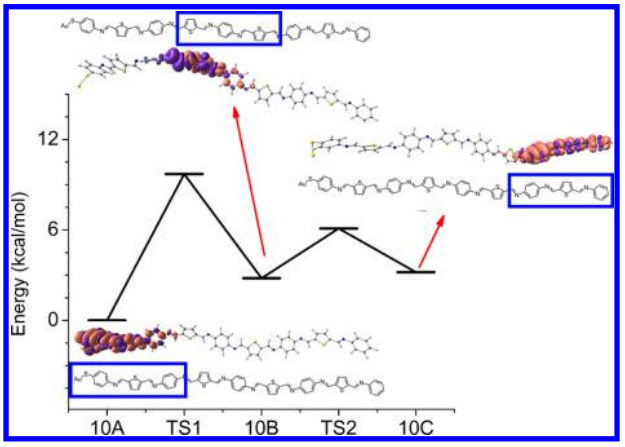

Figure 10. Spin densities and relative energies for three low-energy structures of OPTI-8$^{+\bullet}$ obtained with the M06-HF/TZP level of theory. Energies for transition-state structures are also shown along the reaction coordinate.

Evolution of **10A** to **10B** is calculated to be endoergic by ~3 kcal/mol (0.13 eV) while **10B** and **10C** are predicted to be degenerate in energy to within the accuracy of the DFT model. We optimized a transition-state structure connecting **10A** and **10B** (labeled **TS1** along the reaction coordinate in Figure 10), which has a delocalization of the spin density over about 5 rings, and is characterized by a flattening of the dihedral angle between the third and fourth rings. The barrier for this effective hopping process is calculated to be 9.7 kcal/mol (0.42 eV). This is in reasonable agreement with the empirical hopping activation energy of 8.0 ± 0.5 kcal/mol (0.35 ± 0.03 eV).

While hole transport across the OPTI-8 wire by evolution of **10A** to **10C** via **10B** is one possible means to effect charge transport, and an interesting one insofar as the charge moves three ring registers with each hop, there are many low-energy structures for OPTI-8$^{+\bullet}$, prompting us to investigate additional possible hopping mechanisms. In particular, we found three structures corresponding to the shift of the polaron by a single ring register from a starting point having localization similar to **10B** (Figure 11). The starting structure is nearly isoenergetic with **10B**, and sequentially evolves to two other structures, through barriers of 7.9 kcal/mol (0.34 eV) and 7.4 kcal/mol (0.32 eV), to effect a total register shift of two ring units for the polaron. These values are similar to the value of 9.7 kcal/mol (0.42 eV) obtained for the initial step in the 3-ring register shifts depicted in Figure 10, as well as to the experimental value of 8.0 ± 0.5 kcal/mol (0.35 ± 0.03 eV). Given the very large number of possible structures and their still larger number of possible connections via one-, two-, and three-ring register hops (four and larger seem unlikely given the delocalization length of the polaron), it is not practical to exhaustively characterize all possible transport pathways, but it is encouraging that theory predicts the activation energies to span a reasonably narrow range, and moreover to encompass the experimentally measured value, which presumably reflects averaging over many possible paths, potentially influenced by condensed-phase constraints not present in the computations. Of course, actual charge hopping is an electronic phenomenon that has the potential to take place in a nonadiabatic fashion, but the Born–Oppenheimer energies associated with the minima and transition-state structures are still useful measures of the expected thermal fluctuations that will be required to make even such nonadiabatic transitions probable.

Theory supports, then, that for OPTI-1$^{+\bullet}$ through OPTI-4$^{+\bullet}$, the calculated spin densities of the radical cations are delocalized across the entire wire. The delocalization lengths in the radical cations are thus somewhat greater than might otherwise be predicted from consideration only of the HOMOs of the neutral, preionized precursors (Figure 5). Such long delocalization lengths are consistent with tunneling from one electrode to the other in these shorter wires. By contrast, in the electronic ground states of the cations OPTI-5$^{+\bullet}$ through OPTI-8$^{+\bullet}$, the spin densities for alternative local minima are highly localized to subregions of the molecular wire, i.e.,

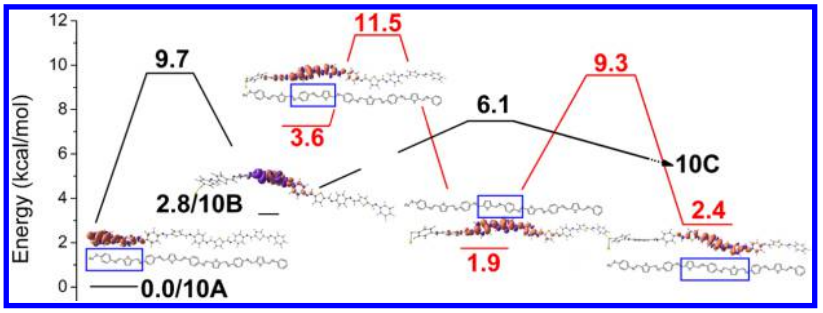

Figure 11. Spin densities and relative energies for various low-energy structures of OPTI-8$^{+\bullet}$ obtained with the M06-HF/TZP level of theory. The scheme in which the spin-density evolves in 1-ring shifts is indicated in red while the scheme involving 3-ring shifts (reproducing Figure 10) is indicated in black. For clarity, the starting point of the red curve is shown shifted upward from its energy of 3.6 kcal/mol.

DOI: 10.1021/jacs.5b07400
J. Am. Chem. Soc. XXXX, XXX, XXX–XXX

polarons are formed. The spin densities of the lowest energy structures obtained for OPTI-$n^{+\bullet}$ (n = 5, 6 and 7) are presented in Figure S11. This is consistent with hole transport occurring primarily by charge hopping with characteristic activation energy and mobility increasing with temperature. For the longer wires, we find a polaron length of roughly three rings and calculated barriers in reasonable agreement with experimental measurements.

Despite the larger resistance of these wires compared to OPI wires,[39] the activation energies are comparable to what we have measured before in other oligoimine systems (0.38 eV versus 0.4−0.6 eV).[40,41,68] This suggests that the rate-determining step of the hopping transport is similar not only in the longer lengths of the OPTI wires but also between different oligoimine molecular wire structures. The 30-fold decrease in conductivity compared to the OPI wires (1×10^{-5} S cm^{-1}) can be attributed to several factors. Less planarity in the molecular backbone could hinder charge delocalization, which is apparent in the experimental optical and electrochemical spectra as well as in the DFT calculations. Also, if the charge has to hop through each unit in the wire, then having structurally different units adjacent to each other should reduce the exchange interaction for charge transfer between units (noting here that unit may not necessarily imply only a single ring). Dell, Capozzi and DuBay et al. have measured the conductance of short thiophene-containing molecules along with phenylene analogues using the STM break junction method, and their findings suggest that the molecule's rotational degrees of freedom (which are fewer for the thiophene-containing molecule compared to the phenylene analogue) are structure dependent and impact the conductance.[69] The asymmetric structure of the OPTI wires and the 2−3 molecules/nm^2 coverage of the SAM could sterically hinder some of the rotations, as shown in Figure S12, and reduce the conductivity. Further systematic studies into the effects of rotational barriers and energy level matching between subunits on the charge hopping process in long molecular wires is an important future direction.

There is also still much to learn about interfacial charge transfer in molecular junctions. We have focused this investigation on charge transport within the wires, but electronic phenomena at the metal−organic interface is also an essential part of the contact-to-contact transport process. Interfacial dipoles arising from chemical and physical metal-molecule contacts play an important role here.[70,7] Contact-to-molecule charge transfer can result in orbital level shifts and transport gap renormalization through image-charge effects.[71] These effects can be subtle and require carefully designed experimental and theoretical investigation, but are crucial to construct a complete picture of hopping transport in these systems.

CONCLUSION

We have demonstrated the controlled, sequential growth of molecular wires incorporating the thiophene moiety. The structural and electrical properties of these wires have been characterized to determine fundamental relationships with molecular wire length. Electrical transport measurements show that charge transport in short OPTI oligomers is temperature independent, while for longer oligomers it is activated, consistent with a crossover from tunneling to hopping transport as wire length increases. It is clear from the optical and electrochemical measurements that the electronic structure changes very little with length beyond OPTI-3, indicating that charge is not delocalized across the entire wire length. This conclusion is also supported by DFT calculations that indicate the formation of polarons spanning several adjacent rings. DFT calculations also reveal polaronic transition states with activation energies in good agreement with measured values (0.2−0.4 eV). In total, the experimental and computational results are consistent with a multistep, semiclassical adiabatic hole transfer mechanism within the wires. However, the calculations indicate that there are several possible pathways involving intramolecular register shifts of various lengths for polarons. Further theoretical and experimental work to address the details of this process at the molecular level will be informative, particularly with respect to the influence of molecular architecture and deformation on polaron size, formation energy and mobility.

ASSOCIATED CONTENT

Supporting Information

The Supporting Information is available free of charge on the ACS Publications website at DOI: 10.1021/jacs.5b07400.

Additional figures and discussions for the thin film characterization, electrical measurements and details of computational methods and Cartesian coordinates of the structures of the OPTI-n wires. (PDF)

AUTHOR INFORMATION

Corresponding Authors

*frisbie@umn.edu
*cramer@umn.edu
*gagliard@umn.edu

Notes

The authors declare no competing financial interest.

ACKNOWLEDGMENTS

We thank NSF (CHE-1213876) for financial support of the experimental work. Parts of this work were carried out in the Characterization Facility, University of Minnesota, which receives partial support from NSF through the MRSEC program. The computational work (S.O.O., S.G., C.J.C., L.G.) was supported by the U.S. Department of Energy, Office of Science, Office of Advanced Scientific Computing Research, Scientific Discovery through Advanced Computing (SciDAC) program under Award Number DE-SC0008666, and also the Minnesota Supercomputing Institute (MSI) at the University of Minnesota.

REFERENCES

(1) Xu, B. Q.; Li, X. L.; Xiao, X. Y.; Sakaguchi, H.; Tao, N. J. *Nano Lett.* **2005**, *5* (7), 1491−1495.
(2) Ishii, H.; Sugiyama, K.; Ito, E.; Seki, K. *Adv. Mater.* **1999**, *11* (8), 605−625.
(3) Braun, S.; Salaneck, W. R.; Fahlman, M. *Adv. Mater.* **2009**, *21* (14), 1450−1472.
(4) Kim, T.; Darancet, P.; Widawsky, J. R.; Kotiuga, M.; Quek, S. Y.; Neaton, J. B.; Venkataraman, L. *Nano Lett.* **2014**, *14* (2), 794−798.
(5) Bruot, C.; Hihath, J.; Tao, N. J. *Nat. Nanotechnol.* **2012**, *7*, 35−40.
(6) Baldea, I.; Xie, Z.; Frisbie, C. D. *Nanoscale* **2015**, *7*, 10465−10471.
(7) Xie, Z.; Baldea, I.; Smith, C. E.; Wu, Y.; Frisbie, C. D. *ACS Nano* **2015**, *9* (8), 8022−8036.

DOI: 10.1021/jacs.5b07400
J. Am. Chem. Soc. XXXX, XXX, XXX−XXX

(8) Fan, F. R. F.; Yang, J. P.; Cai, L. T.; Price, D. W.; Dirk, S. M.; Kosynkin, D. V.; Yao, Y. X.; Rawlett, A. M.; Tour, J. M.; Bard, A. J. *J. Am. Chem. Soc.* **2002**, *124*, 5550−5560.
(9) Selzer, Y.; Cabassi, M. A.; Mayer, T. S.; Allara, D. L. *J. Am. Chem. Soc.* **2004**, *126*, 4052−4053.
(10) Selzer, Y.; Cabassl, M. A.; Mayer, T. S.; Allara, D. L. *Nanotechnology* **2004**, *15*, S483−S488.
(11) Kang, B. K.; Aratani, N.; Lim, J. K.; Kim, D.; Osuka, A.; Yoo, K. H. *Chem. Phys. Lett.* **2005**, *412*, 303−306.
(12) Tran, E.; Grave, C.; Whitesides, G. A.; Rampi, M. A. *Electrochim. Acta* **2005**, *50*, 4850−4856.
(13) Troisi, A.; Ratner, M. A. *Small* **2006**, *2*, 172−181.
(14) Chen, X.; Jeon, Y. M.; Jang, J. W.; Qin, L.; Huo, F.; Wei, W.; Mirkin, C. A. *J. Am. Chem. Soc.* **2008**, *130*, 8166−8168.
(15) Seitz, O.; Vilan, A.; Cohen, H.; Hwang, J.; Haeming, M.; Schoell, A.; Umbach, E.; Kahn, A.; Cahen, D. *Adv. Funct. Mater.* **2008**, *18*, 2102−2113.
(16) Nozaki, D.; Girard, Y.; Yoshizawa, K. *J. Phys. Chem. C* **2008**, *112*, 17408−17415.
(17) DiBenedetto, S. A.; Facchetti, A.; Ratner, M. A.; Marks, T. J. *J. Am. Chem. Soc.* **2009**, *131*, 7158−7168.
(18) Lu, Q.; Liu, K.; Zhang, H. M.; Du, Z. B.; Wang, X. H.; Wang, F. S. *ACS Nano* **2009**, *3*, 3861−3868.
(19) McCreery, R. L. *ChemPhysChem* **2009**, *10*, 2387−2391.
(20) Okamoto, S.; Morita, T.; Kimura, S. *Langmuir* **2009**, *25*, 3297−3304.
(21) Tuccitto, N.; Ferri, V.; Cavazzini, M.; Quici, S.; Zhavnerko, G.; Licciardello, A.; Rampi, M. A. *Nat. Mater.* **2009**, *8*, 41−46.
(22) Yamada, R.; Kumazawa, H.; Tanaka, S.; Tada, H. *Appl. Phys. Express* **2009**, *2*, 3.
(23) Simeone, F. C.; Rampi, M. A. *Chimia* **2010**, *64*, 362−369.
(24) Sedghi, G.; Sawada, K.; Esdaile, L. J.; Hoffmann, M.; Anderson, H. L.; Bethell, D.; Haiss, W.; Higgins, S. J.; Nichols, R. J. *J. Am. Chem. Soc.* **2008**, *130*, 8582−8583.
(25) Yamada, R.; Kumazawa, H.; Noutoshi, T.; Tanaka, S.; Tada, H. *Nano Lett.* **2008**, *8*, 1237−1240.
(26) Xing, Y. J.; Park, T. H.; Venkatramani, R.; Keinan, S.; Beratan, D. N.; Therien, M. J.; Borguet, E. *J. Am. Chem. Soc.* **2010**, *132*, 7946−7956.
(27) Li, X.; Hihath, J.; Chen, F.; Masuda, T.; Zang, L.; Tao, N. J. *J. Am. Chem. Soc.* **2007**, *129*, 11535−11542.
(28) Segal, D.; Nitzan, A.; Davis, W. B.; Wasielewski, M. R.; Ratner, M. A. *J. Phys. Chem. B* **2000**, *104*, 3817−3829.
(29) Segal, D.; Nitzan, A. *Chem. Phys.* **2001**, *268*, 315−335.
(30) Berlin, Y. A.; Hutchison, G. R.; Rempala, P.; Ratner, M. A.; Michl, J. *J. Phys. Chem. A* **2003**, *107*, 3970−3980.
(31) Grozema, F. C.; Siebbeles, L. D. A.; Warman, J. M.; Seki, S.; Tagawa, S.; Scherf, U. *Adv. Mater.* **2002**, *14*, 228−231.
(32) Nitzan, A. J. *J. Phys. Chem. A* **2001**, *105*, 2677−2679.
(33) Prins, P.; Grozema, F. C.; Schins, J. M.; Patil, S.; Scherf, U.; Siebbeles, L. D. A. *Phys. Rev. Lett.* **2006**, *96*, 146601.
(34) Davis, W. B.; Svec, W. A.; Ratner, M. A.; Wasielewski, M. R. *Nature* **1998**, *396*, 60−63.
(35) Weiss, E. A.; Ahrens, M. J.; Sinks, L. E.; Gusev, A. V.; Ratner, M. A.; Wasielewski, M. R. *J. Am. Chem. Soc.* **2004**, *126*, 5577−5584.
(36) Nitzan, A. *Annu. Rev. Phys. Chem.* **2001**, *52*, 681−750.
(37) Joachim, C.; Ratner, M. A. *Proc. Natl. Acad. Sci. U. S. A.* **2005**, *102* (25), 8801−8808.
(38) Asadi, K.; Kronemeijer, A. J.; Cramer, T.; Koster, L. J. A.; Blom, P. W. M.; de Leeuw, D. M. *Nat. Commun.* **2013**, *4*, 1710.
(39) Choi, S. H.; Kim, B.; Frisbie, C. D. *Science* **2008**, *320*, 1482.
(40) Choi, S. H.; Frisbie, C. D. *J. Am. Chem. Soc.* **2010**, *132*, 16191.
(41) Luo, L.; Benameur, A.; Brignou, P.; Choi, S. H.; Rigaut, S.; Frisbie, C. D. *J. Phys. Chem. C* **2011**, *115*, 19955−19961.
(42) Bauerle, P.; Fischer, T.; Bidlingmeier, B.; Stabel, A.; Rabe, J. P. *Angew. Chem., Int. Ed. Engl.* **1995**, *34* (3), 303.
(43) Capozzi, B.; Dell, E. J.; Berkelbach, T. C.; Reichman, D. R.; Venkataraman, L.; Campos, L. M. *J. Am. Chem. Soc.* **2014**, *136* (29), 10486−10492.
(44) Yamada, R.; Kumazawa, H.; Tanaka, S.; Tada, H. *Appl. Phys. Express* **2009**, *2*, 3.
(45) Leary, E.; Hobereich, H.; Higgins, S. J.; van Zalinge, H.; Haiss, W.; Nichols, R. J.; Finch, C. M.; Grace, I.; Lambert, C. J.; McGrath, R.; Smerdon, J. *Phys. Rev. Lett.* **2009**, *102*, 086801.
(46) Rosink, J. J. W. M.; Blauw, M. A.; Geerligs, L. J.; van der Drift, E.; Rousseeuw, B. A. C.; Radelaar, S.; Sloof, W. G.; Fakkeldij, E. J. M. *Langmuir* **2000**, *16*, 4547−4553.
(47) Wold, J. D.; Frisbie, C. D. *J. Am. Chem. Soc.* **2001**, *132*, 5549−5556.
(48) Karpe, S.; Ocafrain, M.; Smaali, K.; Lenfant, S.; Vuillaume, D.; Blanchard, P.; Roncali, J. *Chem. Commun.* **2010**, *46*, 3657−3659.
(49) Parikh, A. N.; Allara, D. L.; Ben Azouz, I.; Rondelez, F. *J. Phys. Chem.* **1994**, *98*, 7577−7590.
(50) Zhao, Y.; Truhlar, D. G. *J. Chem. Phys.* **2006**, *125*, 194101.
(51) Zhao, Y.; Truhlar, D. G. *Theor. Chem. Acc.* **2008**, *120*, 215.
(52) Wullen, C. V. *J. Comput. Chem.* **1999**, *20*, 51.
(53) Lenthe, E. V.; Baerends, E. J.; Snijders, J. G. *J. Chem. Phys.* **1993**, *99*, 4597.
(54) Velde, G.; Bickelhaupt, F. M.; Baerends, E. J.; Guerra, C. F.; Gisbergen, S. J. A.; Snijders, J. G.; Ziegler, T. J. *J. Comput. Chem.* **2001**, *22*, 931.
(55) Perdew, J. P.; Burke, K.; Ernzerhof, M. *Phys. Rev. Lett.* **1996**, *77*, 3865−68.
(56) Perdew, J. P.; Burke, K.; Ernzerhof, M. *Phys. Rev. Lett.* **1997**, *78*, 1396.
(57) Grimme, S.; Antony, J.; Ehrlich, S.; Krieg, S. *J. Chem. Phys.* **2010**, *132*, 154104.
(58) Runge, E.; Gross, E. K. *Phys. Rev. Lett.* **1984**, *52*, 997.
(59) Ullrich, C. A.; Gossmann, U. J.; Gross, E. K. U. *Phys. Rev. Lett.* **1995**, *74*, 872.
(60) Tour, J. M.; Jonesll, L.; Pearson, D. L.; Lamba, J. J. S.; Burgin, T. P.; Whitesides, G. M.; Allara, D. L.; Parikh, A. N.; Atre, S. *J. Am. Chem. Soc.* **1995**, *117* (37), 9529−9534.
(61) Shirley, D. A. *Phys. Rev. B* **1972**, *5*, 4709−4714.
(62) Sikes, H. D.; Smalley, J. F.; Dudek, S. P.; Cook, A. R.; Newton, M. D.; Chidsey, C. E. D.; Feldberg, S. W. *Science* **2001**, *291*, 1519−1523.
(63) Demissie, A. T.; Haugstad, G.; Frisbie, C. D. *J. Am. Chem. Soc.* **2015**, *137* (27), 8819−8828.
(64) Bredas, J. L. *Mater. Horiz.* **2014**, *1*, 17−19.
(65) Salomon, A.; Cahen, D.; Lindsay, S.; Tomfohr, J.; Engelkes, V. B.; Frisbie, C. D. *Adv. Mater.* **2003**, *15*, 1881−1890.
(66) Mcreery, R. L.; Bergren, A. J. *Adv. Mater.* **2009**, *21*, 4304−4322.
(67) McCreery, R. L. *Chem. Mater.* **2004**, *16*, 4477−4496.
(68) Choi, S. H.; Risko, C.; Delgado, M. C. R.; Kim, B.; Brédas, J.; Frisbie, C. D. *J. Am. Chem. Soc.* **2010**, *132*, 4358−4368.
(69) Dell, E.; Capozzi, B.; DuBay, K.; Berkelbach, T. C.; Moreno, J. R.; Reichman, D.; Venkataraman, L.; Campos, L. *J. Am. Chem. Soc.* **2013**, *135* (32), 11724−7.
(70) Heimel, G.; Romaner, L.; Zojer, E.; Bredas, J. *Acc. Chem. Res.* **2008**, *41* (6), 721−729.
(71) Perrin, M. L.; Verzijl, C. J. O.; Martin, C. A.; Shaikh, A. J.; Eelkema, R.; van Esch, J. H.; van Ruitenbeek, J. M.; Thijssen, J. M.; van der Zant, H. S. J. *Nat. Nanotechnol.* **2013**, *8*, 282−287.

DOI: 10.1021/jacs.5b07400
J. Am. Chem. Soc. XXXX, XXX, XXX−XXX